

Multidimensional Modelling of Cross-Beam Energy Transfer for Direct-Drive Inertial Confinement Fusion

(Hopefully soon to be Dr.) Philip W. X. Moloney

IMPERIAL

June 2024

Submitted in partial fulfilment of the requirements for the degree of
Doctor of Philosophy of Imperial College London

Department of Physics
Imperial College London
Prince Consort Road
London SW7 2AZ

List of Acronyms

Rad-MHD Radiative-Magnetohydrodynamics

MHD Magnetohydrodynamics

LPIs Laser-Plasma Instabilities

CBET Cross-Beam Energy Transfer

ICF Inertial Confinement Fusion

LLNL Lawrence Livermore National Laboratory

IAW Ion Acoustic Wave

NIF National Ignition Facility

1 Simulations of Cross-Beam Energy Transfer for Magnetised Direct-Drive

This chapter describes a set of simulations which were conducted to understand the role of Cross-Beam Energy Transfer (CBET) in magnetised, direct-drive implosions. Magnetised Inertial Confinement Fusion (ICF) is a promising route to achieving higher target gains, due to the reduction of thermal energy loss at stagnation and additional confinement of the alpha particles responsible for burn propagation. For direct-drive implosions, magnetisation can significantly alter the coronal plasma conditions, due to the introduced anisotropy of thermal transport. The Ion Acoustic Wave (IAW) dispersion relation, which mediates CBET interactions, depends upon the background plasma and therefore significantly altered temperature and density profiles could alter the action of CBET. Before the development of SOLAS, no direct-drive suitable CBET model existed, which was integrated into a Radiative-Magnetohydrodynamics (Rad-MHD) code. Therefore, the CHIMERA-SOLAS framework has enabled the effect of magnetisation on CBET to be studied for a direct-drive implosion.

The chapter begins with a review of experimental and computational work on magnetised ICF, with a particular focus on magnetised direct-drive. Work presented in this chapter focuses on the study of *exploding-pusher* experiments. These are very different implosions to the typical *central hot-spot* ignition designs, presented in previous chapters, so a short summary of exploding pushers is also provided. Simulation results are presented of 1-D and 2-D, unmagnetised exploding pushers, both with and without the effect of CBET, which demonstrate that CBET does significantly alter these implosions. This is followed by an investigation of how various extended-Magnetohydrodynamics (MHD) terms affect the implosion, including the Nernst effect, the Lorentz force and resistive diffusion of the magnetic field. Results are given of how magnetisation affects the CBET interaction and ultimately how it changes the stagnation shape of the target. The results presented, demonstrate that redistribution of deposited power due to CBET reduced the amplitude of the stagnation asymmetry, which originated from the polar beam configuration used. However, the reduction of asymmetry was consistent for different initial seed magnetic field values, and therefore CBET was not observed to be sufficiently strongly affected by magnetisation, to lead to observable signatures in experimental measurements. The chapter concludes with a summary of the work and suggestions of additional experimental configurations, which may leave a more significant signature of magnetisation altering CBET.

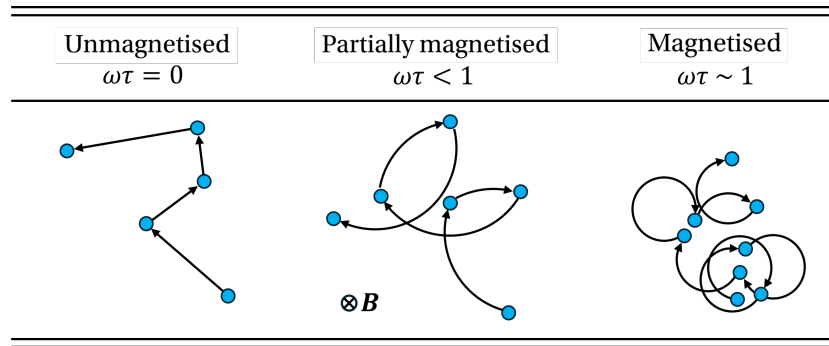


Figure 1.1: Cartoon to illustrate the effect of magnetisation on collisions, and therefore transport, of a test positive charge. Particle locations after collision are represented as blue circles and the path taken by the particle is shown by the black arrows. As the Hall parameter of the particle increases, diffusion is increasingly limited, and therefore collision transport is reduced.

1.1 Magnetised Inertial Confinement Fusion and Exploding Pushers

This chapter begins with a review of published studies of relevance to the work conducted in this chapter. Firstly, a short review of magnetised-ICF is presented, which reviews both the key concepts, existing studies and potential challenges of the design. Both work on direct- and indirect drive is summarised, alongside recent theoretical progress on understanding how magnetisation can effect Laser-Plasma Instabilities (LPIs). The exploding pusher concept is then briefly explored to aid understanding of the implosion physics, which is markedly different to conventional hot-spot ICF.

1.1.1 Potential Benefits of Target Magnetisation

Magnetisation of an ICF target has long been thought of as a potential aid to ignition [1, 2]. It is still a relevant field of study in the context of regular ignition events on the National Ignition Facility (NIF), because by relaxing the ignition threshold, magnetisation could make larger targets feasible at equivalent laser energy, and therefore lead to higher gains than unmagnetised implosions. For a central hotspot ignition targets, ignition occurs when the heat source of alpha energy deposition balances the thermal and radiative losses in the hotspot. Thermal conduction is suppressed perpendicular to magnetic field lines, therefore a magnetic field can reduce thermal losses and aid the power balance required for ignition. Fig. 1.1 demonstrates the effect of increasing magnetisation on a unit positive test charge. By constraining charged particles to orbit field lines, collisional transport terms, such as thermal conduction, are reduced perpendicular to the field direction. Fits of transport coefficients to Fokker-Planck simulations, demonstrate that in a Hydrogen plasma, thermal conductivity perpendicular to field lines κ_{\perp} , is reduced to $\sim 30\%$ of the parallel value κ_{\parallel} at Hall parameter $\omega\tau = 1$, and $\sim 1\%$ at $\omega\tau = 10$ [3]. Thus, for Hall parameters, $\omega\tau \gtrsim 10$, thermal conduction losses are almost negligible in the direction perpendicular to field lines.

Using an order of magnitude estimate for a below ignition threshold hotspot, $T_e \sim 2.5$ keV

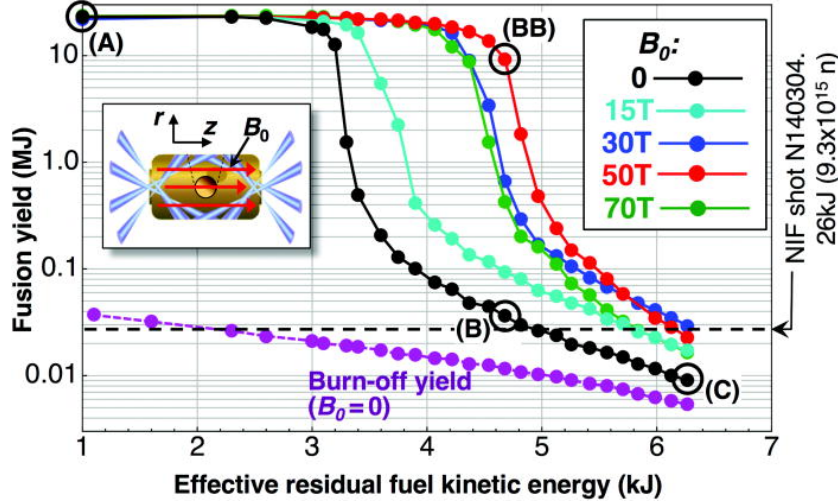


Figure 1.2: Simulated fusion yields versus effective residual fuel kinetic energy under imposed low-mode radiation flux perturbations for imposed fields in the range $B_0 = 0 \rightarrow 70$ (T). The plot demonstrates with increasing departure from ideal compression (moving to the right on the x axis), magnetisation can enable the onset of the ignition. Reused with permission from Ref. [6].

and $\rho \sim 50$ g cm $^{-3}$, a field strength $|\mathbf{B}| \sim 2.5$ kT is required to obtain $\omega\tau \sim 1$ [4]. This field strength cannot be produced directly, but it is possible to produce a smaller field which, assuming frozen in magnetic field and a spherical compression, is amplified by the square of the convergence,

$$|\mathbf{B}_1| = |\mathbf{B}_0| \left(\frac{R_0}{R_1} \right)^2, \quad (1.1)$$

where $|\mathbf{B}_0|$ and $|\mathbf{B}_1|$ are initial and final magnetic fields respectively and R_0 and R_1 are initial and final radii respectively. Laboratory magnetic fields can be produced from pulsed power coils with field strength $|\mathbf{B}| \sim \mathcal{O}(50)$ T [5], so even moderate convergence-ratio targets ($R_0/R_1 \sim 10$) are able to produce strongly magnetised core plasma.

Fig. ?? plots results of magnetised indirect-drive simulations, of a target on the threshold of ignition [6]. Increasing magnitude of radiation perturbation were applied to the drive (moving to the right on the x -axis), which prevent the target from achieving ignition, which is visible as the steep increase in yield, below some threshold level of perturbation. The results demonstrate that when an initial magnetic field was applied to the target, it more robustly ignited with increasing field strength due to reduced conduction losses. This simulation work, prior to the achievement of ignition on the NIF [7], motivated the development of a magnetised ICF campaign at Lawrence Livermore National Laboratory (LLNL) [8].

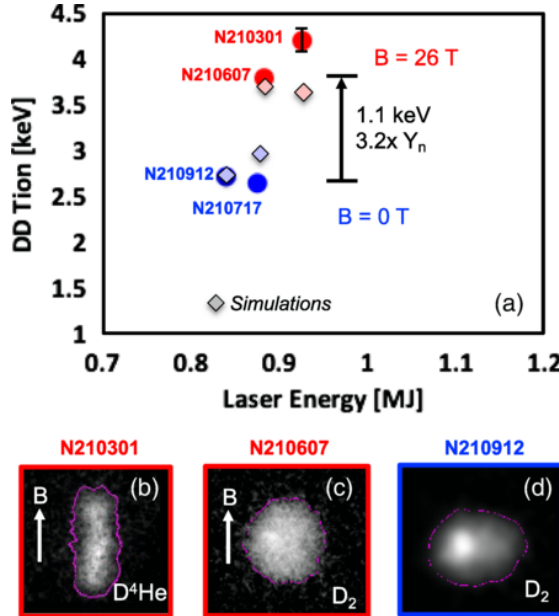


Figure 1.3: a) A 1.1 keV T_i increase was achieved by adding a 26 T B_0 field to a D_2 gas capsule implosion on the NIF. Also shown in the plot are the simulation results. b)–d) Equatorial shapes of the implosions. Reused with permission from Ref. [9].

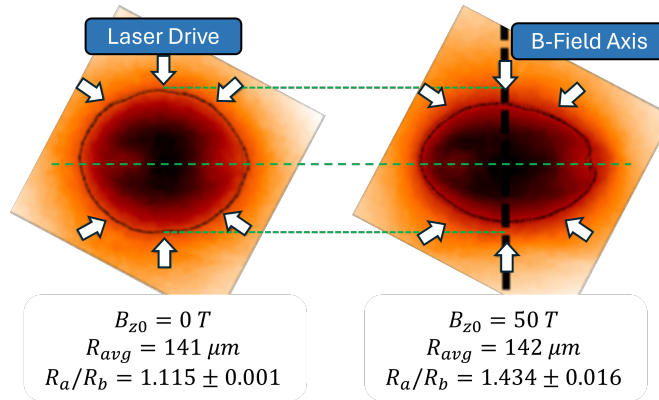


Figure 1.4: X-ray self emission images of (left) an unmagnetised and (right) a magnetised implosion. The average radius of the marked contour (corresponding to 40% of peak intensity), and the oblateness parameter R_a/R_b (ratio of major-to-minor axis) are listed below each image. The polar laser-drive is indicated by the white arrows, and the axis of the initial magnetic field by the black dashed line on the right. Applying an initial magnetic field demonstrated increased oblateness of the implosion. Adapted with permission from Ref. [10].

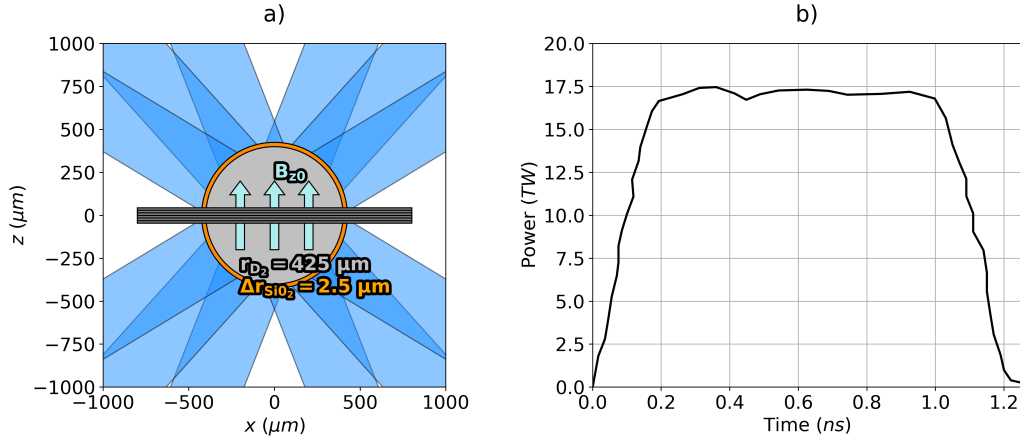


Figure 1.5: The initial conditions used for all simulations presented in this chapter. Panel a) plots the D_2 filled, glass shell capsule and direction of the initial magnetic field. An example field coil (illustrative and not included in simulations) is also shown, the presence of which necessitated the polar laser drive in experiments. Panel b) plots the laser pulse shape used, which had a total of 17.7 kJ laser energy.

1.1.2 Experimental Studies of Magnetised-ICF

1.1.3 Magnetised Laser-Plasma Instabilities

1.1.4 The Exploding-Pusher Configuration

1.2 Effect of Cross-Beam Energy Transfer in Unmagnetised Exploding Pushers

This section presents simulation results of the effect of CBET in exploding pushers on OMEGA. Both 1-D and 2-D CHIMERA-SOLAS simulations of 40-beam, polar driven exploding pusher experiments are presented, with a focus on how CBET acts to change the implosion. The 1-D results demonstrate that CBET significantly reduces the coupled laser energy to the implosion from ... to Simulations conducted in 2-D, with a full 3-D raytrace and CBET model, show that CBET alters spatial profile of the laser deposition, reducing asymmetry in the drive.

1.2.1 Simulation Configuration

1.2.2 1-D Simulations

1.2.3 2-D Simulations

1.3 The Effect of Magnetisation on Exploding-Pusher Implosions

This section presents results of a study of the effect that extended-MHD has on the 2-D exploding pusher simulations. Simulations were conducted with varying initial magnetic field strengths and particular terms turned off and on to deduce what the important physical processes are. Magnetised transport is important for both initial seed magnetic field implosions,

Table 1.1: Results of all Simulations. In the CBET column, ‘~’ indicates CBET acted on the magnitude, but *not* spatial location, of deposition.

Run	Dim.	CBET	Note	B_{z0} (T)	t_b (ns)	$\langle T_i \rangle$ (keV)	Y_n ($\times 10^{10}$)	Δb (ps)	$\frac{R_{\text{equator}}}{R_{\text{pole}}} \Big _{t=t_b}$
1	1-D	Off	-	0	0.69	14.66	11.62	87	$1.00^{+0.00}_{-0.00}$
2	1-D	On	-	0					$1.00^{+0.00}_{-0.00}$
3	2-D	Off	-	0	0.71	8.44	6.20	148	$2.96^{+0.20}_{-0.19}$
4	2-D	~	-	0	0.75	7.61	5.23	153	$3.26^{+0.25}_{-0.23}$
5	2-D	On	-	0	0.75	7.77	5.46	148	$3.23^{+0.25}_{-0.23}$
6	2-D	Off	-	25	0.74	7.26	4.73	130	$3.80^{+0.41}_{-0.33}$
7	2-D	~	-	25	0.78	6.58	4.14	125	$4.55^{+0.50}_{-0.43}$
8	2-D	On	-	25	0.78	6.72	4.44	123	$4.32^{+0.47}_{-0.41}$
9	2-D	Off	-	50	0.73	6.82	3.73	134	$4.40^{+0.43}_{-0.38}$
10	2-D	~	-	50	0.78	6.30	3.30	130	$4.92^{+0.56}_{-0.48}$
11	2-D	On	-	50	0.78	6.37	3.52	129	$4.79^{+0.55}_{-0.47}$
12	2-D	Off	No Aniso.	25	0.81	6.40	5.02	118	$3.14^{+0.68}_{-0.50}$
13	2-D	Off	No Lor.	25	0.74	7.29	4.77	131	$3.80^{+0.41}_{-0.33}$
14	2-D	Off	No Nern.	25	0.73	7.41	4.85	130	$3.74^{+0.38}_{-0.32}$
15	2-D	Off	No Resis.	25	0.73	7.07	4.59	132	$3.84^{+0.42}_{-0.33}$

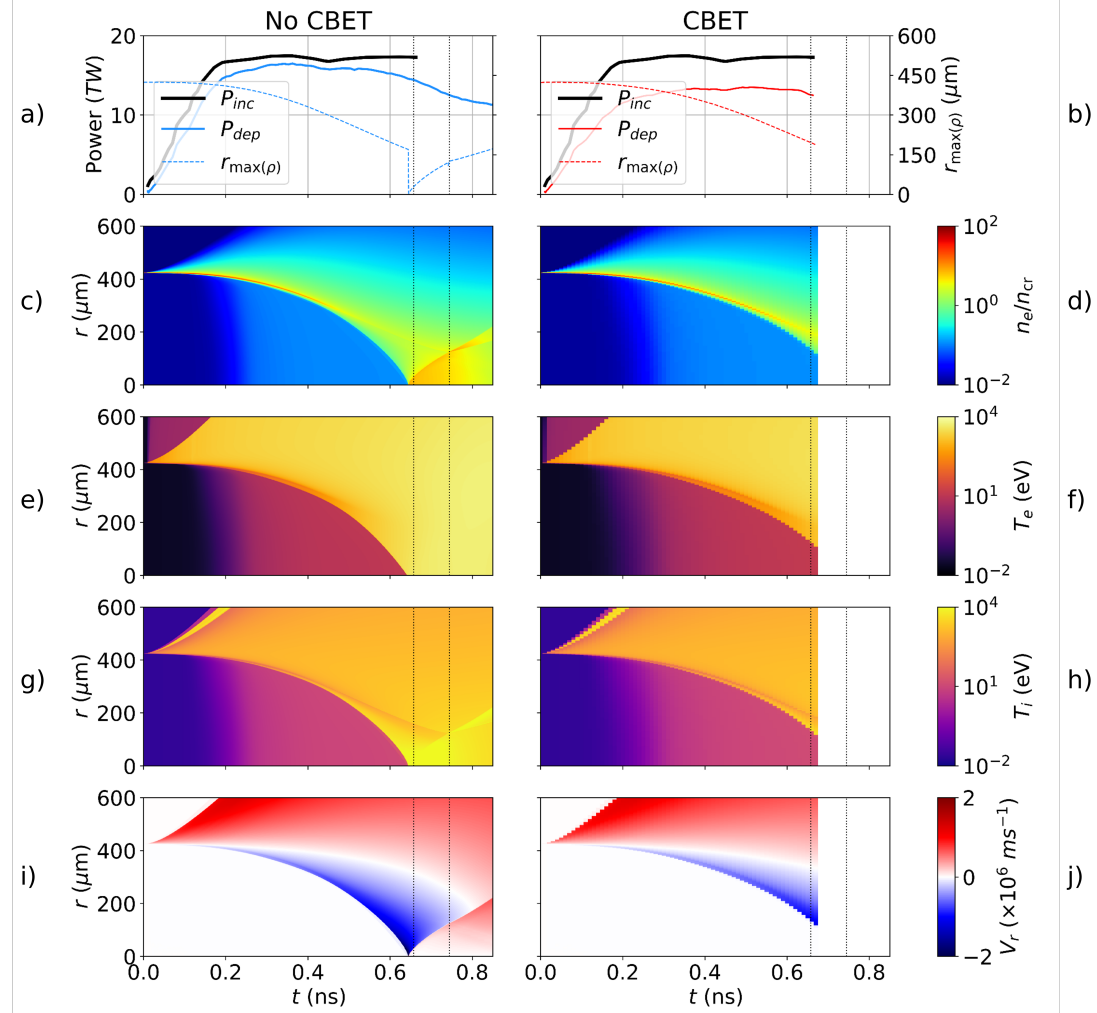


Figure 1.6: 1-D Simulation results both without (left) and with (right) CBET. The top row plots the incident and absorbed energy from the simulation on the left axis and the radius of maximum density on the right. In order, the next rows plot n_e , T_e , T_i and V_r . The full-width half-maximum times of the D_2 yield are plotted as dotted vertical black lines on all panels.

resulting in large coronal Hall parameters and therefore significant anisotropy of the implosions. The results demonstrate that (resistive diffusion and the Lorentz force have very little impact on the implosion physics, due to the bulk of the plasma being highly resistive and high- β respectively)?????????????????????. The Nernst advection of magnetic field ??????????????????????

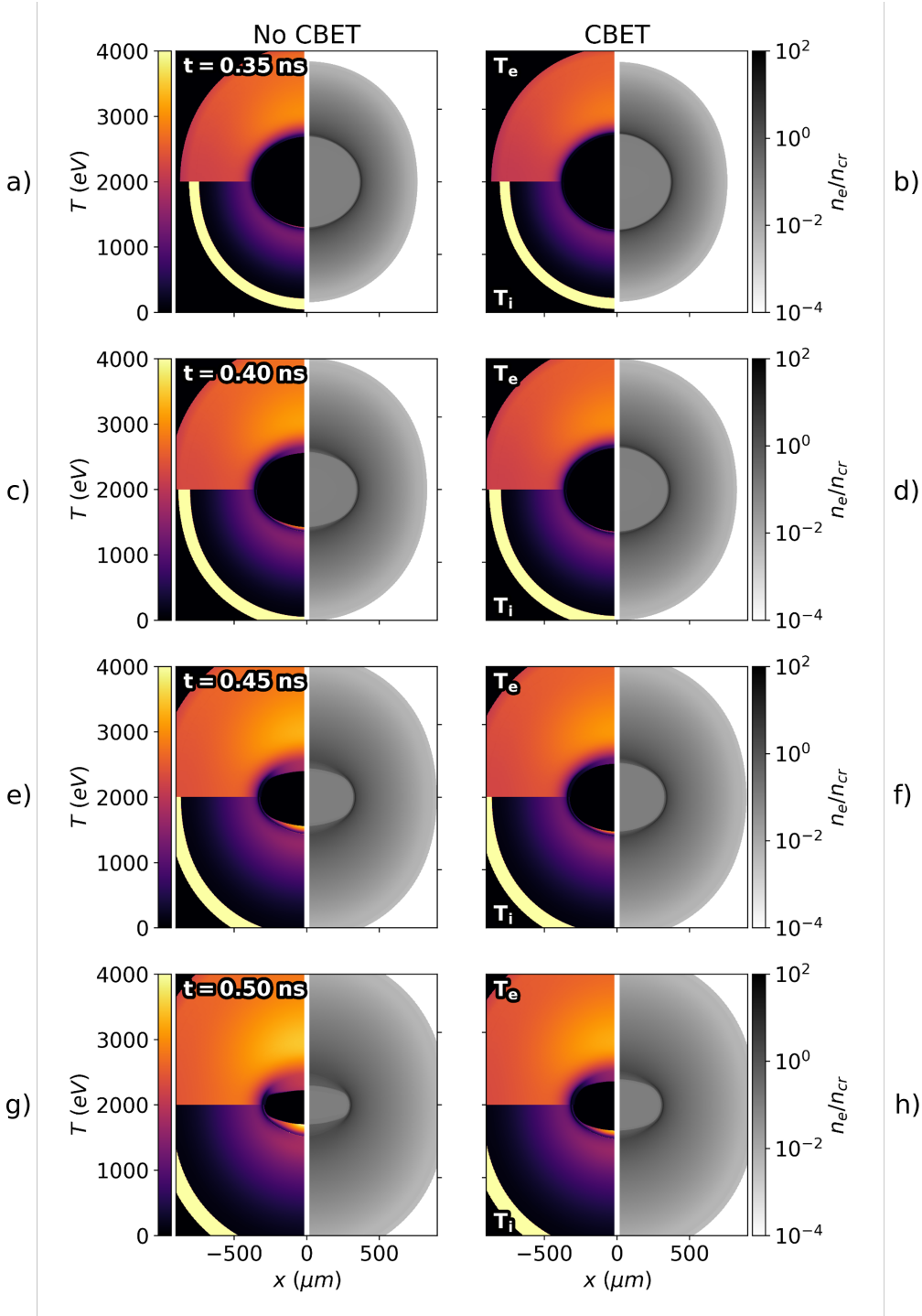


Figure 1.7: n_e (right-side), T_e (top-left-side) and T_i (bottom-left-side) plots from the 2-D, 0 T simulations without (left) and with (right) CBET at a variety of in-flight times. The decreased deposited energy due to CBET, results in lower coronal electron temperatures and therefore a slower, weaker shock being driven, which is especially evident at later times.

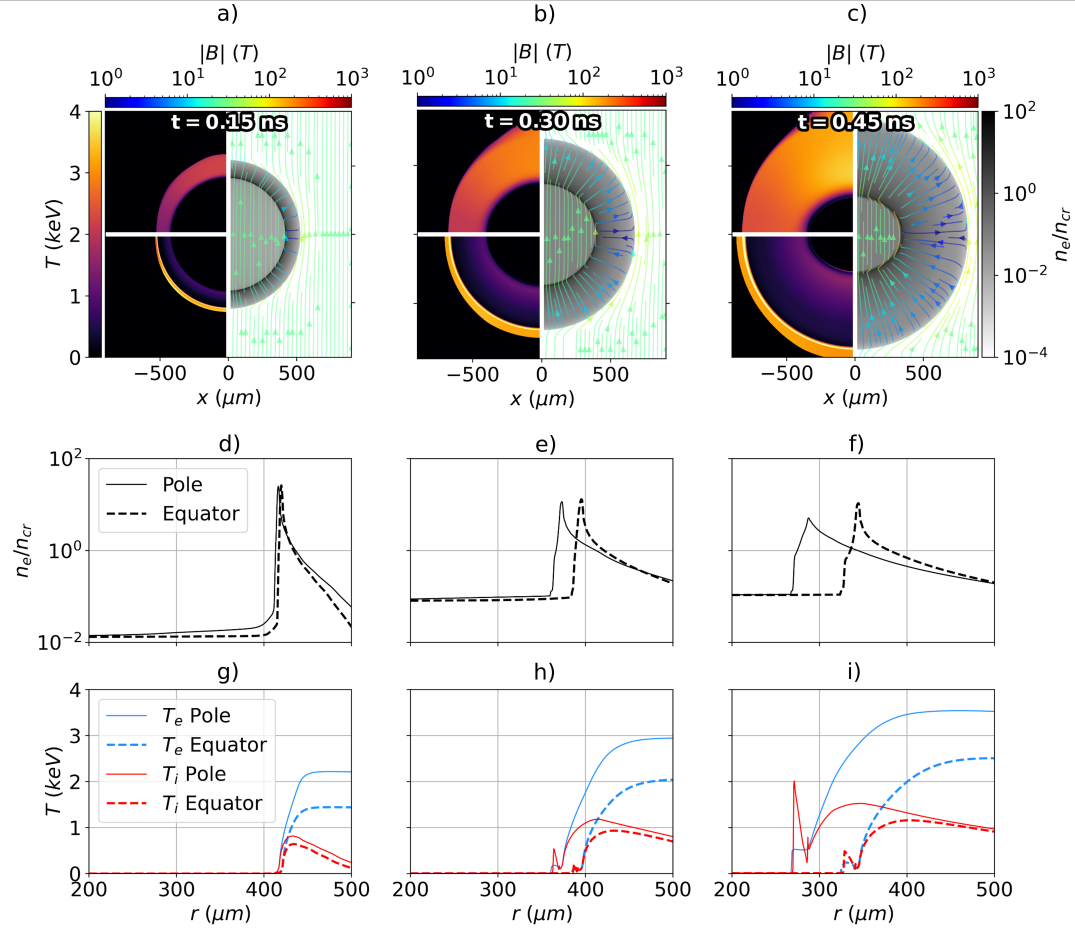


Figure 1.8: The development of the hydrodynamic variables and magnetic field structure from the $B_{z0} = 25$ T, CBET simulation. Panels a), b) and c) plot T_e (top-left), T_i (bottom-left), n_e (right) and \mathbf{B} (streamlines) at $t = 0.15$, 0.30 and 0.45 ns respectively. The approximately radially outward flowing, hot (and therefore highly conductive) ablating plasma pulls the magnetic field with it, resulting in radial \mathbf{B} field lines, which are weaker at the capsule equator. The radial field lines in the corona prevent angular equilibration of temperature, so act to keep heat at the poles. Compression of the SiO_2 shell leads to a non-radial field pile up on the inside edge of the maximum density, which is most clearly visible in panel c). Panels d), e) and f) plot n_e lineouts along the pole ($\theta = 0^\circ$) and equator ($\theta = 90^\circ$). Panels g), h) and i) plot equivalent T_e and T_i lineouts. These all show that the increased polar temperatures, partially due to beam geometry and partially due to magnetisation, lead to preferential ablation at the pole.

1.3.1 In-Flight Field Structure

1.3.2 Anisotropic Thermal Conduction

1.3.3 The Nernst Effect

1.3.4 Resistive Diffusion and the Lorentz Force

1.4 The Effect of Magnetisation on Cross-Beam Energy Transfer and Stagnation

This section presents results on how the magnetisation of the corona affects both CBET scattering and the stagnation shape of the implosion. As was shown in the previous sections, the

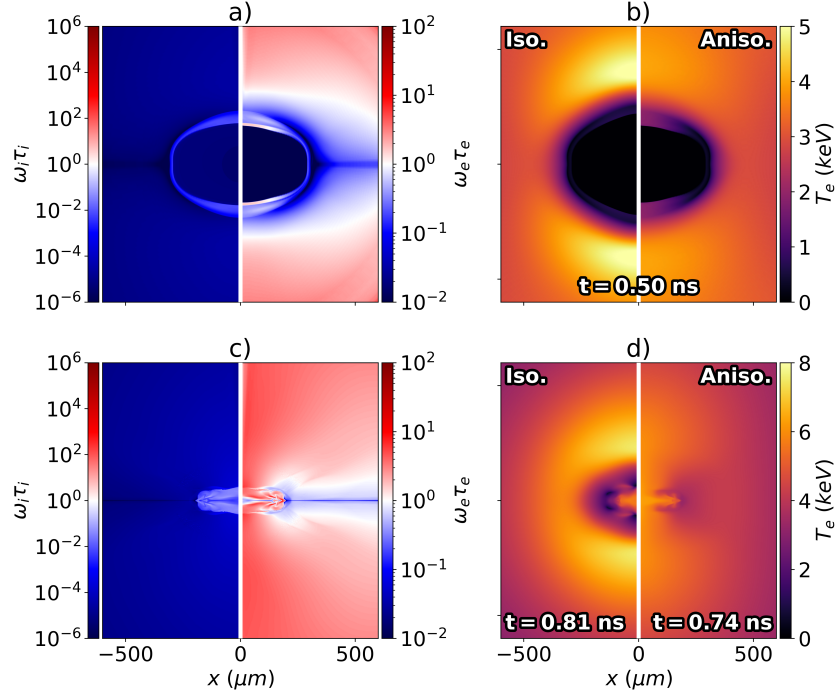


Figure 1.9: In-flight a) and bangtime c) Hall parameters, from the $B_{z0} = 25$ T, no-CBET, anisotropic conduction simulation. Panel b) plots the T_e from the isotropically magnetised simulation (left-side) and anisotropic conduction simulation (right-side) in-flight. Panel c) plots the T_e from the isotropically magnetised simulation (left-side) and anisotropic conduction simulation (right-side) at peak neutron production. The electron Hall parameter is > 1 at the poles due to high magnetic fields and temperatures, leading to significantly restricted thermal conduction from magnetised transport at the poles. Isotropically magnetised conduction (*i.e.* setting $\kappa_{\parallel} = \kappa_{\perp}$), therefore results in a markedly different implosion morphology, as is shown in panels b) and d). Ion hall parameters peak at bangtime, with values reaching about $\omega_i \tau_i \sim 0.1$.

laser geometry leads to a significant mode $\ell = 2$ in the coronal plasma conditions, which is significantly amplified by anisotropic thermal conduction when magnetised. This long-wavelength perturbation is slightly reduced by CBET, consistent with existing literature on how CBET mitigates $\ell = 1$ asymmetries [11]. ‘No-CBET’ simulations were conducted, for which the coupled energy was kept the same as the equivalent CBET simulation, *i.e.* so CBET only acted to redistribute the deposited power, rather than reduce its magnitude. These results showed that the increasingly anisotropic coronal plasma profiles for increasing seed magnetic field strengths did lead to changes in the CBET scattering, this was too small an effect to lead to experimentally observable changes in behaviour.

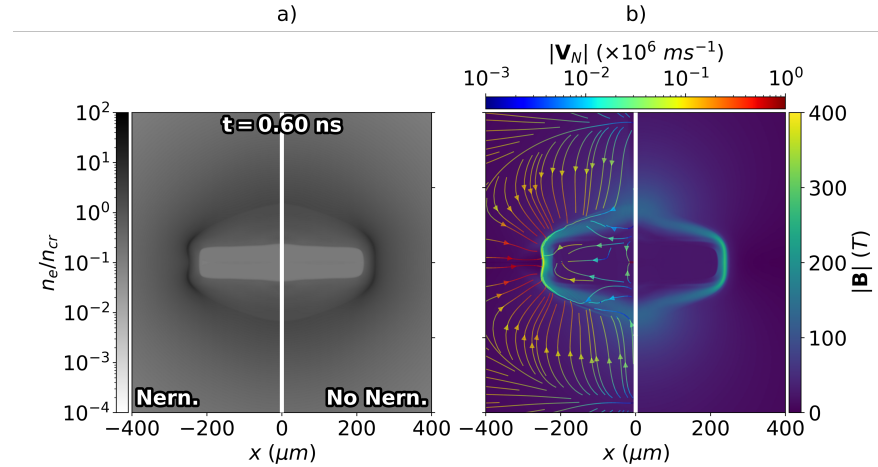


Figure 1.10: Panel a) plots in-flight electron density profiles from the $B_{z0} = 25 \text{ T}$, no-CBET simulations with (left-side) and without (right-side) Nernst advection of the magnetic field. Panel b) plots magnetic field magnitude from the Nernst (left-side) and no-Nernst (right-side) simulation. The Nernst advection velocity is also plotted for the Nernst simulation as streamlines, coloured by speed. Advection of the field is important in the low Hall parameter equatorial region, pulling \mathbf{B} down ∇T_e , into the dense wall. Altered field at the equator impacts on the magnetised thermal conduction, which ultimately imprints on the density, as is seen in panel a).

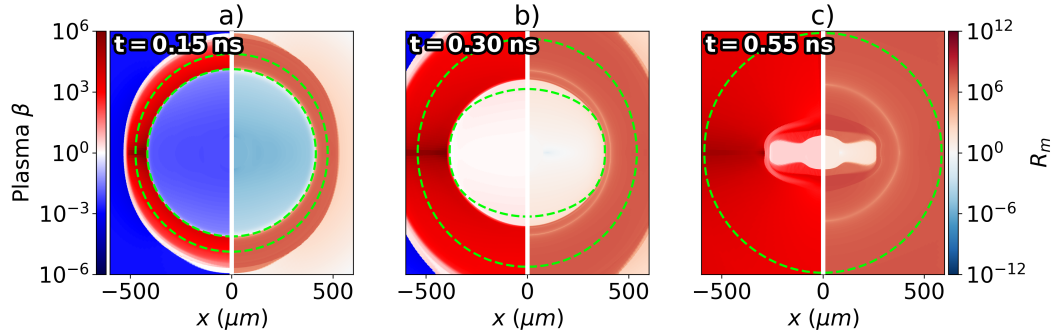


Figure 1.11: Plasma β (left-side) and Magnetic Reynolds Number, R_m , (right-side) at various in-flight times, throughout the $B_{z0} = 25 \text{ T}$, no-CBET simulation. Contours of the $n_e = n_{cr}/10$ are plotted on all panels as dashed green lines to indicate the bounding region containing a significant amount plasma. Broadly, the β and R_m values are $\gg 1$ in all regions with an appreciable amount of plasma, which demonstrate that the Lorentz force and resistive diffusion respectively, should have minimal effect on the implosion dynamics.

1.4.1 Analysis and Key Definitions

1.4.2 Spatial Change of CBET and Deposition from Magnetisation

1.4.3 Stagnation Profiles

If CBET was anisotropically affected by magnetisation, this would result in spatial differences in deposition location, between the full CBET (top row) and CBET-on-magnitude sim-

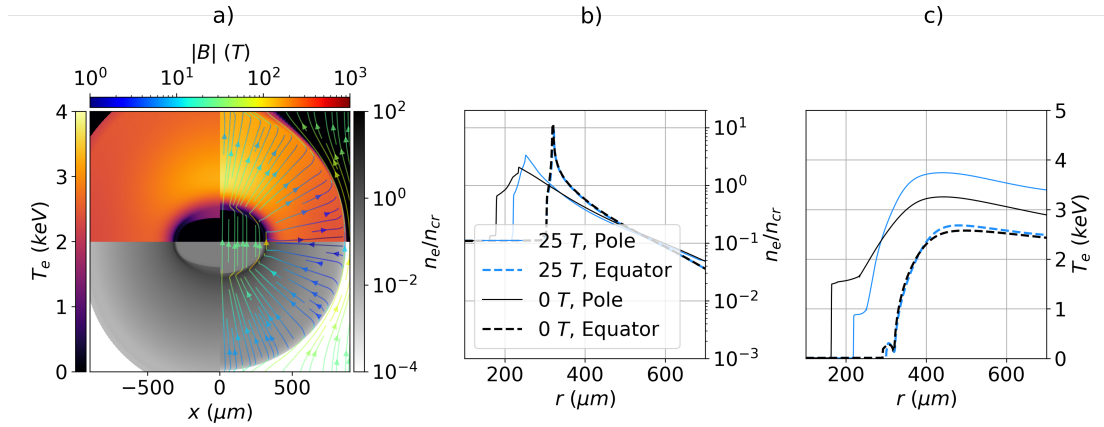


Figure 1.12: Comparison of n_e and T_e profiles from the $B_{z0} = 0$ (panel a) left-side) and 25 T (panel a) right-side), with-CBET simulations, both at $t = 0.5$ ns. Panel a) also plots streamlines of \mathbf{B} for the $B_{z0} = 25$ T simulation, coloured by the field magnitude. Panels b) and c) plot n_e and T_e lineouts respectively, along both the pole and equator. It is evident from these lineouts that magnetisation anisotropically affects hydrodynamic variables, which are used to calculate the CBET gain. Therefore, it is anticipated that magnetisation could anisotropically affect the CBET scattering volume.

ulations (middle row), and therefore the bangtime profiles could be different. Additionally, higher initial magnetisation increases the anisotropy of the coronal plasma and therefore

1.5 Conclusions

1.5.1 Summary of Work

1.5.2 Future Work

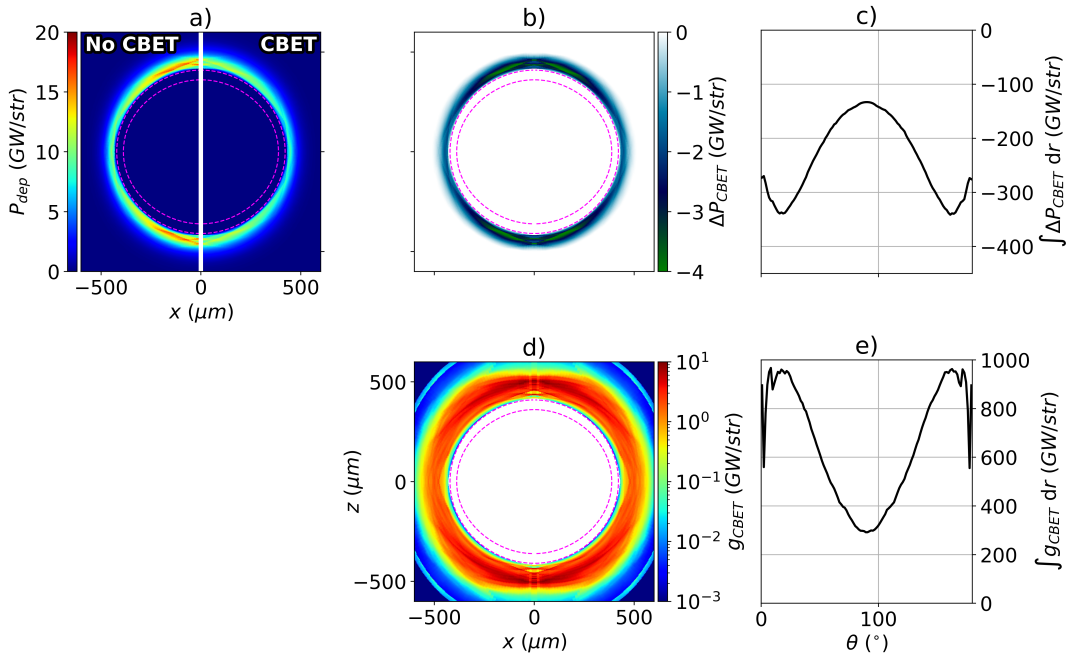


Figure 1.13: Various CBET diagnostics used in the analysis presented in this section. All plots are from the $B_{z0} = 0$ T, with-CBET simulation at $t = 0.30$ ns. Panel a) plots the instantaneous deposition with (right-side) and without (left-side) the effect of CBET. The ‘CBET-deficit’, ΔP_{CBET} , which is the no-CBET deposition, subtracted from the with-CBET deposition, is plotted in panel b). Panel c) plots the radially integrated ΔP_{CBET} , as a function of polar angle. The ‘CBET-scattering’, defined in Eq. ??, is plotted in panel d), and the radial integral is plotted in panel e). At this time, it is evident from panel e) that more CBET occurs at the capsule poles, resulting in a CBET-reduction of deposition near the poles, seen in panel c).

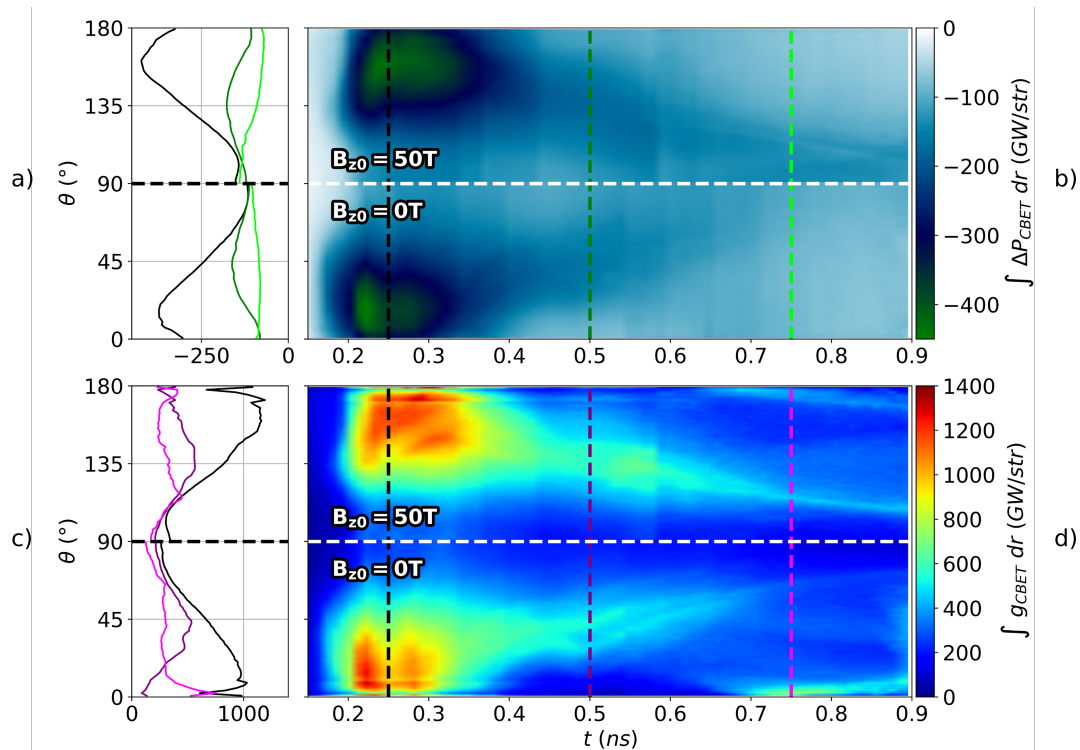


Figure 1.14: The radially integrated CBET-deficit and CBET-scattering, plotted as a function of angle and time for the $B_{z0} = 0$ and 50T , with-CBET simulations. Panel b) plots the CBET-deficit from the 50T (top-half) and 0T (bottom-half) simulations. Lineouts in θ at $t = 0.25$ (black), 0.50 (dark-green) and 0.75 ns (light-green) are plotted in panel a). The same results, but for CBET-scattering are plotted in panels d) and c). It is evident from these plots that for both simulations, as time progresses and the poles of the capsule fall in faster than the equator, the region where CBET mostly occurs, shifts in angle around the capsule. Differences are visible in all plots between the $B_{z0} = 0$ and 50T simulations, indicating that magnetisation affected CBET indirectly, via the altered hydrodynamics.

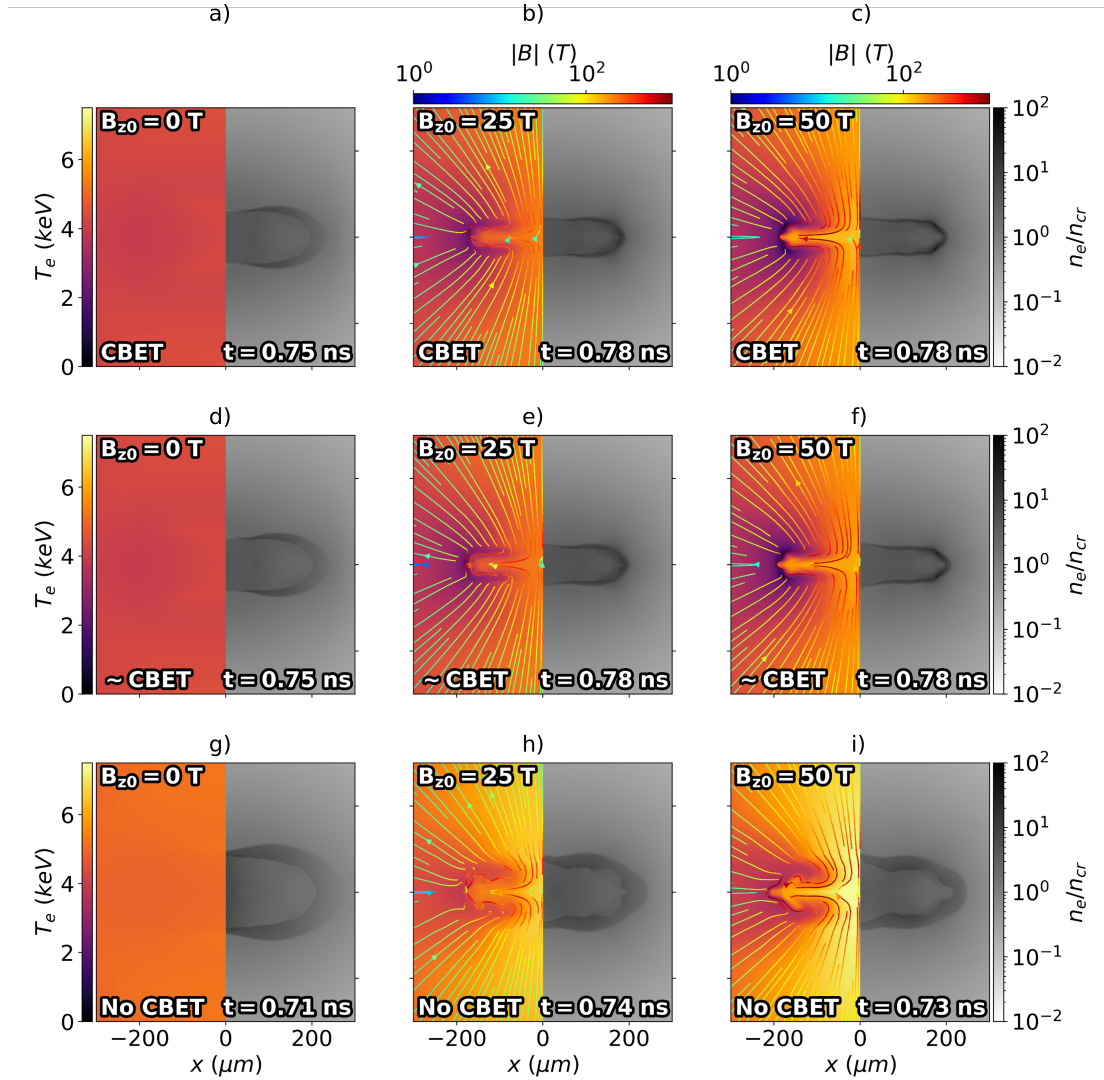


Figure 1.15: n_e , T_e and \mathbf{B} profiles from the time of peak neutron production for different initial magnetisation (columns) and CBET effects (rows). Panels a), b) and c) are from the full CBET simulations, which show that magnetisation increases the oblateness of the stagnation profile. Panels d), e) and f) are from the simulations where only the CBET effect on the magnitude, but not spatial location, of deposition was included. These simulations have identical coupled energy to the top row, and therefore have the same bangtimes. Panels g), h) and i) are from the no-CBET simulations, which have earlier bangtimes and increased temperatures due to the higher coupled energy.

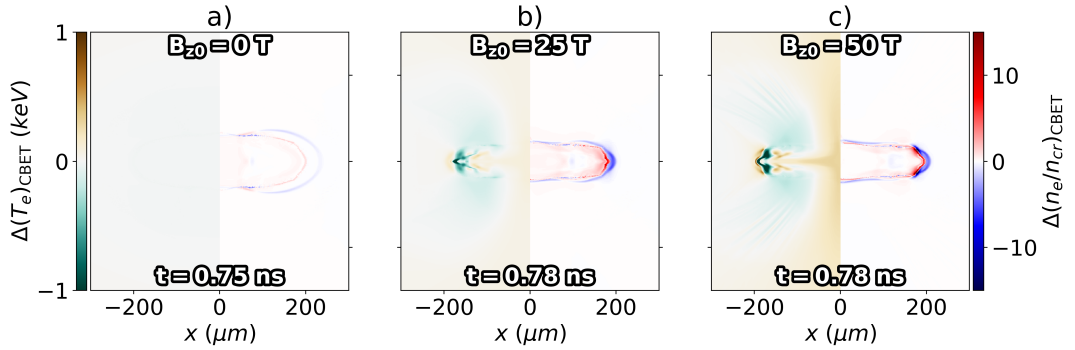


Figure 1.16: Difference in n_e and T_e bangtime profiles, between the full-CBET and CBET-magnitude a) $B_{z0} = 0$ T, b) $B_{z0} = 25$ T and c) $B_{z0} = 50$ T simulations. The difference in variable ν , $\Delta\nu$ is the $\nu_{full-CB} - \nu_{magCB}$, so higher colour scale values represent regions with increased ν for the full CBET calculation. These results primarily show that CBET slightly reduces the bangtime equatorial radius, and thus reduces the oblateness, compared to simulations where the spatial redistribution of power due to CBET is neglected.

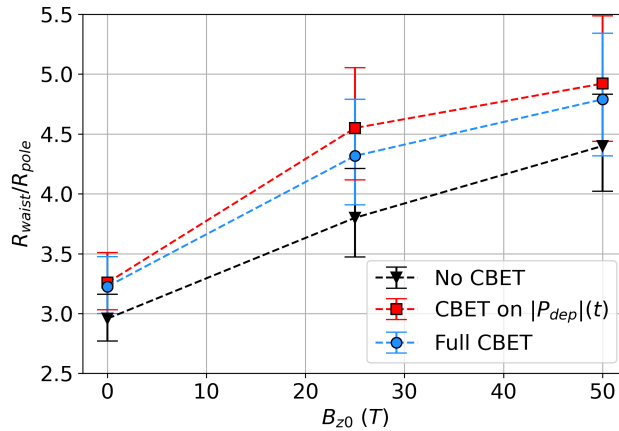


Figure 1.17: The oblateness of bangtime density profiles for different magnetisation and CBET effects. All values and errors were obtained by fitting an ellipse (with axes orientated along \hat{x} and \hat{z}), to the radius of maximum density. No-CBET simulations are consistently more round, because the initial shock is stronger and therefore travels ahead of the pusher material more quickly than the CBET equivalent. Thus, after rebounding off the axis, it meets the infalling mass and produces thermonuclear conditions at a larger radius. As was seen in Fig. 1.16, throughout the entire implosion, when including the effect of CBET on spatial location of deposition, it acts to slightly move energy from the pole to the waist and thus marginally reduces oblateness of the implosion.

Appendices

Bibliography

- [1] I.R. Lindemuth and R.C. Kirkpatrick. Parameter space for magnetized fuel targets in inertial confinement fusion. *Nuclear Fusion*, 23(3):263–284, March 1983. ISSN 0029-5515, 1741-4326. doi: 10.1088/0029-5515/23/3/001. URL <https://iopscience.iop.org/article/10.1088/0029-5515/23/3/001>. 6
- [2] R.D. Jones and W.C. Mead. The physics of burn in magnetized deuterium-tritium plasmas: spherical geometry. *Nuclear Fusion*, 26(2):127–137, February 1986. ISSN 0029-5515, 1741-4326. doi: 10.1088/0029-5515/26/2/001. URL <https://iopscience.iop.org/article/10.1088/0029-5515/26/2/001>. 6
- [3] E. M. Epperlein and M. G. Haines. Plasma transport coefficients in a magnetic field by direct numerical solution of the Fokker-Planck equation. *The Physics of Fluids*, 29(4):1029–1041, April 1986. ISSN 0031-9171. doi: 10.1063/1.865901. URL <https://pubs.aip.org/pfl/article/29/4/1029/819331/Plasma-transport-coefficients-in-a-magnetic-field>. 6
- [4] Sam Thomas Jack O'Neill. *Modelling Ignition and Burn in Pre-magnetised Inertial Confinement Fusion Experiments*. PhD thesis, Imperial College London, London, December 2023. 7
- [5] G. Fiksel, A. Agliata, D. Barnak, G. Brent, P.-Y. Chang, L. Folnsbee, G. Gates, D. Hasset, D. Lonobile, J. Magoon, D. Mastrosimone, M. J. Shoup, and R. Betti. Note: Experimental platform for magnetized high-energy-density plasma studies at the omega laser facility. *Review of Scientific Instruments*, 86(1):016105, January 2015. ISSN 0034-6748, 1089-7623. doi: 10.1063/1.4905625. URL <https://pubs.aip.org/rsi/article/86/1/016105/360963/Note-Experimental-platform-for-magnetized-high>. 7
- [6] L. J. Perkins, D. D.-M Ho, B. G. Logan, G. B. Zimmerman, M. A. Rhodes, D. J. Strozzi, D. T. Blackfield, and S. A. Hawkins. The potential of imposed magnetic fields for enhancing ignition probability and fusion energy yield in indirect-drive inertial confinement fusion. *Physics of Plasmas*, 24(6):062708, June 2017. ISSN 1070-664X, 1089-7674. doi: 10.1063/1.4985150. URL <https://pubs.aip.org/pop/article/24/6/062708/108192/The-potential-of-imposed-magnetic-fields-for>. 7
- [7] A. B. Zylstra, O. A. Hurricane, D. A. Callahan, A. L. Kritcher, J. E. Ralph, H. F. Robey, J. S. Ross, C. V. Young, K. L. Baker, D. T. Casey, T. Döppner, L. Divol, M. Hohenberger, S. Le Pape, A. Pak, P. K. Patel, R. Tommasini, S. J. Ali, P. A. Amendt, L. J. Atherton, B. Bachmann, D. Bailey, L. R. Benedetti, L. Berzak Hopkins, R. Betti, S. D. Bhandarkar,

- J. Biener, R. M. Bionta, N. W. Birge, E. J. Bond, D. K. Bradley, T. Braun, T. M. Briggs, M. W. Bruhn, P. M. Celliers, B. Chang, T. Chapman, H. Chen, C. Choate, A. R. Christoperson, D. S. Clark, J. W. Crippen, E. L. Dewald, T. R. Dittrich, M. J. Edwards, W. A. Farmer, J. E. Field, D. Fittinghoff, J. Frenje, J. Gaffney, M. Gatu Johnson, S. H. Glenzer, G. P. Grim, S. Haan, K. D. Hahn, G. N. Hall, B. A. Hammel, J. Harte, E. Hartouni, J. E. Heebner, V. J. Hernandez, H. Herrmann, M. C. Herrmann, D. E. Hinkel, D. D. Ho, J. P. Holder, W. W. Hsing, H. Huang, K. D. Humbird, N. Izumi, L. C. Jarrott, J. Jeet, O. Jones, G. D. Kerbel, S. M. Kerr, S. F. Khan, J. Kilkenny, Y. Kim, H. Geppert Kleinrath, V. Geppert Kleinrath, C. Kong, J. M. Koning, J. J. Kroll, M. K. G. Kruse, B. Kustowski, O. L. Landen, S. Langer, D. Larson, N. C. Lemos, J. D. Lindl, T. Ma, M. J. MacDonald, B. J. MacGowan, A. J. Mackinnon, S. A. McLaren, A. G. MacPhee, M. M. Marinak, D. A. Mariscal, E. V. Marley, L. Masse, K. Meaney, N. B. Meezan, P. A. Michel, M. Millot, J. L. Milovich, J. D. Moody, A. S. Moore, J. W. Morton, T. Murphy, K. Newman, J.-M. G. Di Nicola, A. Nikroo, R. Nora, M. V. Patel, L. J. Pelz, J. L. Peterson, Y. Ping, B. B. Pollock, M. Ratledge, N. G. Rice, H. Rinderknecht, M. Rosen, M. S. Rubery, J. D. Salmonson, J. Sater, S. Schiaffino, D. J. Schlossberg, M. B. Schneider, C. R. Schroeder, H. A. Scott, S. M. Sepke, K. Sequoia, M. W. Sherlock, S. Shin, V. A. Smalyuk, B. K. Spears, P. T. Springer, M. Stadermann, S. Stoupin, D. J. Strozzi, L. J. Suter, C. A. Thomas, R. P. J. Town, E. R. Tubman, C. Trosseille, P. L. Volegov, C. R. Weber, K. Widmann, C. Wild, C. H. Wilde, B. M. Van Wonterghem, D. T. Woods, B. N. Woodworth, M. Yamaguchi, S. T. Yang, and G. B. Zimmerman. Burning plasma achieved in inertial fusion. *Nature*, 601(7894):542–548, January 2022. ISSN 1476-4687. doi: 10.1038/s41586-021-04281-w. URL <https://www.nature.com/articles/s41586-021-04281-w>. Publisher: Nature Publishing Group. 7
- [8] J. D. Moody, B. B. Pollock, H. Sio, D. J. Strozzi, D. D.-M. Ho, C. Walsh, G. E. Kemp, S. O. Kucheyev, B. Kozioziemski, E. G. Carroll, J. Kroll, D. K. Yanagisawa, J. Angus, S. D. Bhandarkar, J. D. Bude, L. Divol, B. Ferguson, J. Fry, L. Hagler, E. Hartouni, M. C. Herrmann, W. Hsing, D. M. Holunga, J. Javedani, A. Johnson, D. Kalantar, T. Kohut, B. G. Logan, N. Masters, A. Nikroo, N. Orsi, K. Piston, C. Provencher, A. Rowe, J. Sater, K. Skulina, W. A. Stygar, V. Tang, S. E. Winters, J. P. Chittenden, B. Appelbe, A. Boxall, A. Crilly, S. O'Neill, J. Davies, J. Peebles, and S. Fujioka. The Magnetized Indirect Drive Project on the National Ignition Facility. *Journal of Fusion Energy*, 41(1): 7, June 2022. ISSN 0164-0313, 1572-9591. doi: 10.1007/s10894-022-00319-7. URL <https://link.springer.com/10.1007/s10894-022-00319-7>. 7
- [9] J. D. Moody, B. B. Pollock, H. Sio, D. J. Strozzi, D. D.-M. Ho, C. A. Walsh, G. E. Kemp, B. Lahmann, S. O. Kucheyev, B. Kozioziemski, E. G. Carroll, J. Kroll, D. K. Yanagisawa, J. Angus, B. Bachmann, S. D. Bhandarkar, J. D. Bude, L. Divol, B. Ferguson, J. Fry, L. Hagler, E. Hartouni, M. C. Herrmann, W. Hsing, D. M. Holunga, N. Izumi, J. Javedani, A. Johnson, S. Khan, D. Kalantar, T. Kohut, B. G. Logan, N. Masters, A. Nikroo, N. Orsi, K. Piston, C. Provencher, A. Rowe, J. Sater, K. Skulina, W. A. Stygar, V. Tang, S. E. Winters, G. Zimmerman, P. Adrian, J. P. Chittenden, B. Appelbe, A. Boxall, A. Crilly,

- S. O'Neill, J. Davies, J. Peebles, and S. Fujioka. Increased Ion Temperature and Neutron Yield Observed in Magnetized Indirectly Driven D₂-Filled Capsule Implosions on the National Ignition Facility. *Physical Review Letters*, 129(19):195002, November 2022. ISSN 0031-9007, 1079-7114. doi: 10.1103/PhysRevLett.129.195002. URL <https://link.aps.org/doi/10.1103/PhysRevLett.129.195002>. 8
- [10] A. Bose, J. Peebles, C. A. Walsh, J. A. Frenje, N. V. Kabadi, P. J. Adrian, G. D. Sutcliffe, M. Gatū Johnson, C. A. Frank, J. R. Davies, R. Betti, V. Yu. Glebov, F. J. Marshall, S. P. Regan, C. Stoeckl, E. M. Campbell, H. Sio, J. Moody, A. Crilly, B. D. Appelbe, J. P. Chittenden, S. Atzeni, F. Barbato, A. Forte, C. K. Li, F. H. Seguin, and R. D. Petrasso. Effect of Strongly Magnetized Electrons and Ions on Heat Flow and Symmetry of Inertial Fusion Implosions. *Physical Review Letters*, 128(19):195002, May 2022. ISSN 0031-9007, 1079-7114. doi: 10.1103/PhysRevLett.128.195002. URL <https://link.aps.org/doi/10.1103/PhysRevLett.128.195002>. 8
- [11] A. Colaïtis, I. Igumenshchev, J. Mathiaud, and V. Goncharov. Inverse ray tracing on icosahedral tetrahedron grids for non-linear laser plasma interaction coupled to 3D radiation hydrodynamics. *Journal of Computational Physics*, 443:110537, October 2021. ISSN 0021-9991. doi: 10.1016/j.jcp.2021.110537. URL <https://www.sciencedirect.com/science/article/pii/S0021999121004320>. 14

Permissions